Arabian Journal of Geosciences (2020) 13:832
https://doi.org/10.1007/s12517-020-05849-y

ORIGINAL PAPER

ASTER spectral band ratios for lithological mapping: a case study for measuring geological offset along the Erkenek Segment of the East Anatolian Fault Zone, Turkey

Abdelrahman Khalifa[1,3] · Ziyadin Çakır[1] · Şinasi Kaya[2] · Safwat Gabr[4]

Received: 9 June 2019 / Accepted: 12 August 2020

Abstract

The current work examines the lithological variation along the Erkenek Segment of the East Anatolian Fault (EAF), a major tectonic structure which accommodates the westward extrusion of Anatolia together with the North Anatolian Fault. Mapping the geology at high spatial resolution along this segment with conventional mapping techniques is highly challenging due to the complex tectonic setting and the abundant number of different lithological units of varying spatial extent. Therefore, in the current study, the Advanced Spaceborne Thermal Emission and Reflection Radiometer (ASTER) data along the Erkenek Segment have been used different spectral rationing techniques are applied with band the ratios of 1/3–1/9–3/9, 7/3–1/7–3/5 and 9/5–5/3–3/1 being remarkably useful for detailed lithological mapping and hence detecting the geological offsets along this section of the fault. Thus, these ASTER band ratio images can be used for the lithological mapping along the whole EAF and on other regions in the world with similar lithological and geomorphological conditions.

Keywords Band ratios · Geological offsets · ASTER · Remote sensing · East Anatolian Fault

Introduction

The sinistral East Anatolian Fault (EAF) extends for about 400 km between Karlıova triple junction in the northeast and Maraş triple junction in the southwest, characterizing the boundary between the Anatolian and Arabian plates in eastern Turkey (Mckenzie 1970; Şengör et al. 1985; Dewey et al. 1986) (Fig. 1). The age of the EAF is suggested to be the latest Miocene to earliest Pliocene (Hempton 1985; Şengör et al. 1985). Depending on the detailed geological mapping along the EAF, the offsets on the pre-Miocene rocks are measured between 14 and 26 km (Herece 2008; Hubert-Ferrari et al. 2009; Duman and Emre 2013). In terms of recent activity of this fault zone, the GPS-based geodetic models and palaeoseismological studies yield a slip rate of about 10 mm/year (Meghraoui et al. 2006; Reilinger et al. 2006; Aktuğ et al. 2016). Additionally, the morphotectonic analysis of the EAF zone confirms that the fault zone possesses different degrees (medium to high) of tectonic activities (Khalifa 2018; Khalifa et al. 2019).

The EAF is divided by Duman and Emre (2013) and Khalifa et al. (2018) into five segments, which are, from east to west, called Karlıova, Palu, Pütürge, Erkenek, and Pazarcık, respectively (Fig. 2). The Erkenek Segment is a 62-km-long geometric fragment of the EAF, which is delimited from the Pütürge Segment with a restraining double bend at Çelikhan and from the Pazarcık Segment with a releasing step-over at Gölbaşı (Duman and Emre 2013) (Fig. 2). The rugged topography and the complex geology of this segment suggest this zone as an ideal deformed region to apply multispectral remote sensing analyses for examining its total deformation. During the last decade, application of remote sensing techniques was widely used in lithological and structural geology mapping, especially in the tectonically active regions (Khalifa

Responsible Editor: Biswajeet Pradhan

✉ Abdelrahman Khalifa
akhalifa@azhar.edu.eg

[1] Department of Geological Engineering, Faculty of Mines, Istanbul Technical University, Istanbul, Turkey

[2] Department of Geomatic, Faculty of Engineering, Istanbul Technical University, Istanbul, Turkey

[3] Department of Geology, Faculty of Science, Al-Azhar University, Cairo, Egypt

[4] National Authority for Remote Sensing and Space Sciences, Cairo, Egypt

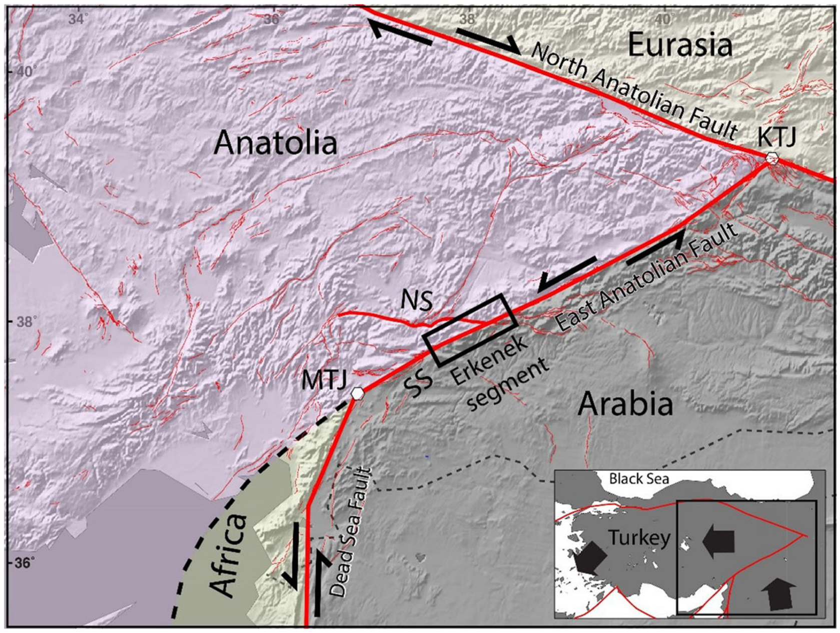

Fig. 1 Shaded relief image (data from SRTM-30; Farr et al. 2007) of eastern Turkey showing the African, Arabian, Anatolian, and Eurasian lithospheric plates and major active faults (thick red lines). MTJ, Maraş triple junction; KTJ, Karliova triple junction; MS, main strand; NS, northern strand of the East Anatolian Fault. The black box shows location of the study fault segment

2014; Pour and Hashim 2015; Ibrahim et al. 2016; Liu et al. 2017; Khalifa 2018; Pour et al. 2018c; Bacheri et al. 2019; Nemmour-Zekiri and Oulebsir 2020). For the geological mapping purposes, ASTER data has a great advantage because it is a unique combination of the wide spectral coverage and the high spatial resolution of the visible and near-infrared bands (Gad and Kusky 2007). The ASTER satellite images are recorded in 14 spectral bands with different wavelength ranges: three bands in visible and near-infrared (VNIR) with 15 m spatial resolution, six bands in short-wave infrared (SWIR) with 30 m spatial resolution, and five bands in thermal infrared (TIR) with 90 m spatial resolution. Relatively multinumbered bands of ASTER satellite images and their wide wavelength ranges are ideal for making a distinguishment between broad ranges of lithological compositions (Gad and Kusky 2007). ASTER data is well known to have been used in many geological and tectonic applications (e.g., Bedell 2001; Rowan et al. 2003; Ninomiya et al. 2005; Gad and Kusky 2007; Gürsoy et al. 2017). In comparison with other datasets such as Landsat TM and ETM+ images, ASTER data provide a great innovation regarding their higher spatial resolution and improved spectral characteristics (e.g., Okada and Ishii 1993; Bedell 2001; Rowan and Mars 2003; Velosky et al. 2003; Gad and Kusky 2007; Rajendran et al. 2013; Gürsoy et al. 2017). Hence, in the same track of Landsat TM and ETM+, ASTER band ratio combinations and band math are successful in emphasizing spectral features of certain rock units and minerals and therefore are more effective in lithological mapping compared with the RGB band combination images (Okada and Ishii 1993; Abdeen et al. 2001; Bedell 2001; Hewson et al. 2001; Rowan and Mars 2003; Rowan et al. 2003; Velosky et al. 2003; Gad and Kusky 2007). Although the ASTER data enhance the efficiency to discriminate the boundaries between the different lithological units, the VNIR bands have been successfully used in vegetation and iron-oxide/hydroxide minerals mapping (Bedell 2001; Pour et al. 2018a; 2018d; Sheikhrahimi et al. 2019), whereas the spectral SWIR bands are very useful for soil and lithological mapping (Yamaguchi

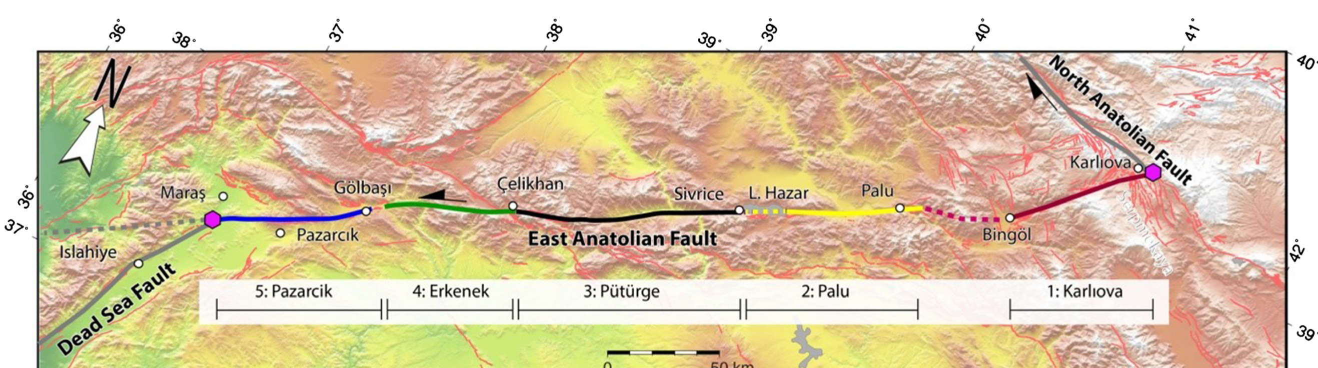

Fig. 2 Segmentation of the East Anatolian Fault following Duman and Emre (2013). Pink hexagons indicate the location of the Karliova and Maraş triple junctions

and Naito 2003) and have a very good ability to trace and map hydrothermal alteration mineral zone associated with ore mineralization (Mars and Rawan 2010; Pour et al. 2013; Gabr et al. 2015; Safari et al. 2017; Pour et al. 2019; Sheikhrahimi et al. 2019). Moreover, the TIR bands are applied specifically to discriminate and map the silicate rocks (Yamaguchi et al. 1998; Ninomiya et al. 2005). In this study, we aim to combine ASTER-based remote sensing analyses with the available field data and statistically detected low levels of spectral information (high optimum index factor (OIF)) in order to refine the geological map of the Erkenek Segment of the EAF, Turkey, and to measure the cumulative offset along this segment. Results from this research will provide valuable information on the evolution, not only for this particular segment but also for the whole EAF as well.

Geological setting

The age of the lithological units along the Erkenek Segment ranges from pre-Cambrian to Holocene time. According to the geological map of Herece (2008) (Fig. 3), the pre-Cambrian Pütürge metamorphic is mostly exposed at the eastern parts of the segment zone. The lower Permian crystallized limestone covers a region in the northern part of the fault and two small elongated parts in the western part of the Erkenek Segment. The Devonian-Carboniferous Yoncayolu Formation includes schist, recrystallized limestone, and quartzite located in the western part of the study area. Calc-schist and schist with marble of the Lower Triassic are found inside the crystallized limestone unit in the northern part of the study area.

The Middle-Upper Triassic-Cretaceous Kayaköy Formation crops out in both sides of the fault and is considered the most important formation in terms of measuring the lateral offset along the fault. This unit is composed of dolomite and rarely crystallized limestone (Herece 2008) (Fig. 3). The Upper Triassic-Cretaceous units are covering most of the southern parts of the study area. The Upper Cretaceous is recognized by Ula Formation that generally distributed in the central and western parts of the area. Ula and Kayaköy formations together in the same unit show one of the geological offsets in the northern part of the Erkenek Segment. The Upper Cretaceous meta-conglomerates characterize the unit of Ula and Kayaköy formations and are very good markers for measuring the lateral segment offsets. The other Upper Cretaceous units that include Berit metaophiolite, Hatay ophiolite, Gulman ophiolite, and granitoids are distributed almost along the fault zone (Herece 2008) (Fig. 3).

The Lower-Middle Eocene rocks are represented by thin elongated bodies of claystone and mudstone in the eastern and upper-middle parts of the study region. Hoya Formation that took place during Lower-Middle Eocene time is composed of neritic and clayey limestone and located in the lower-middle part of the study area. Middle-Upper Eocene is represented by Melefan Formation that includes packstone and olistostrome. The Melefan Formation is recorded in two small parts above the linkage point between the southern and the northern fault strands (Herece 2008) (Fig. 3). Gaziantep Formation belongs to Eocene-Oligocene and consists of chalky and pelagic limestone.

Gaziantep and Hoya formations occupy most of the western part of the study area. Conglomerate, sandstone, and mudstone of the Lower Pleistocene are recorded in the middle northern part of the fault segment. Upper Pleistocene-Holocene lithology crops out along the fault trace line. The Holocene deposits were mapped in the study area as alluvial

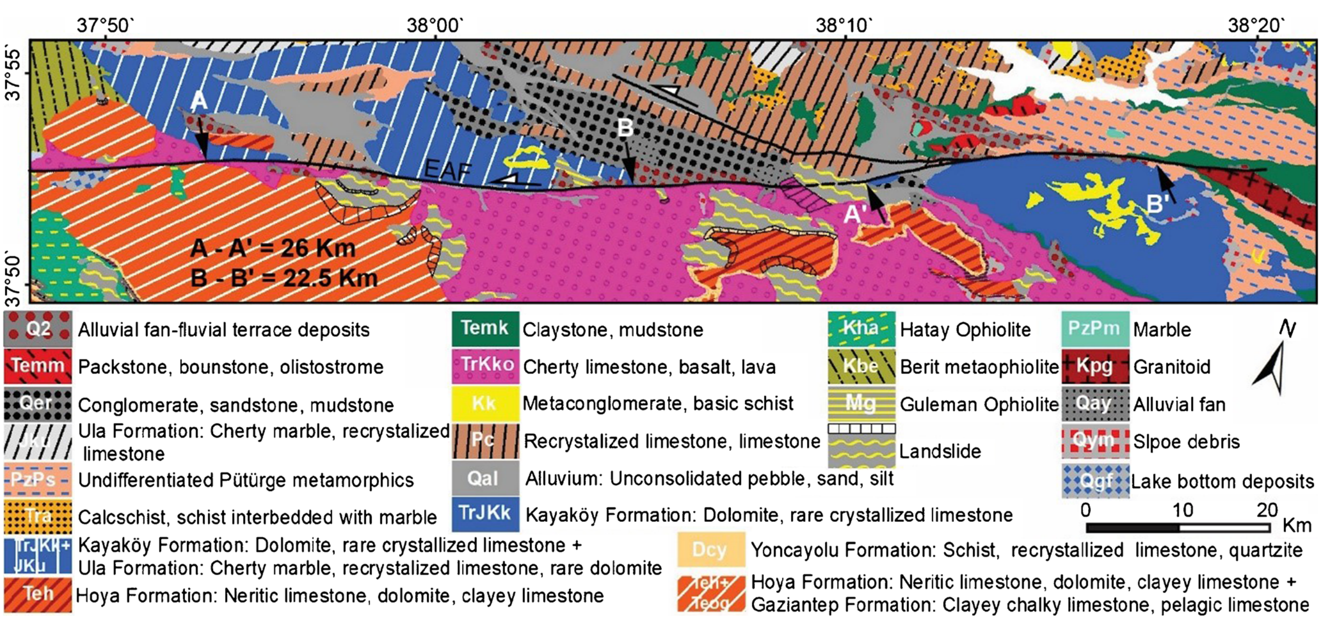

Fig. 3 Geological map of the Erkenek Segment (modified after Herece 2008)

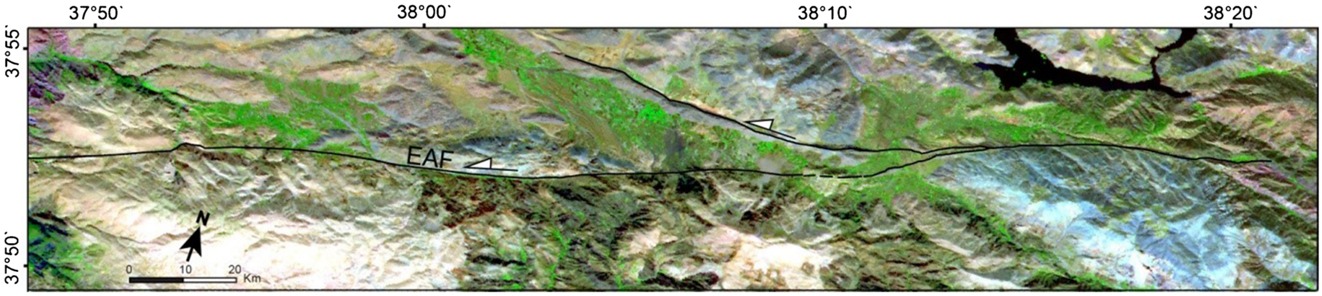

Fig. 4 ASTER 7-3-1 image for Erkenek fault segment region

sediments mostly located in the central section of the fault segment. Slope debris units are recorded in small areas in the northeastern and northwestern parts of the area. Lake bottom deposits are mapped in the western part of the area. Alluvial deposits were recorded in the eastern, middle, and western parts of the fault segment area (Herece 2008) (Fig. 3).

The geological offsets along the Erkenek Segment were measured between Kayaköy Formation in the southern part of the fault segment and the Kayaköy and Hoya formations as a one unit, in the northern part of the fault segment to be 22.5 km and 26 km, respectively, in both measured locations (Herece 2008) (Fig. 3).

Materials and methods

This study examined a cloud free ASTER data which have been obtained from US Geological Survey Earth Resources Observation and Science Centre (EROS) (https://earthexplorer.usgs.gov). Three ASTER level 1T (Precision Terrain Corrected Registered At-Sensor Radiance) scenes covering the Erkenek fault segment were obtained on September 2001. The ASTER level IT data contains calibrated at sensor radiance, which corresponds with the ASTER data level 1B that has been geometrically corrected and rotated to a north up UTM projection. The images investigated in this study have been pre-georeferenced to UTM zone 37 North projection with the WGS-1984 datum.

Cross-talk correction was applied on the ASTER data as a pre-processing step to reduce the SWIR cross-talk effect, which is caused by dispersion of band 4 detector incident light to other SWIR detectors (Iwasaki and Tonooka 2005; Mars and Rawan 2010; Sheikhrahimi et al. 2019). The 30 m resolution SWIR dataset were layer-stacked and re-sampled to correspond to the VNIR dataset forming images with 15 m of spatial resolution. Band rationing technique was selected to examine the study fault segment, which is characterized by high exposed areas of rugged terrains. This technique is working well with arid and semi-arid regions; hence, ASTER band ratio was very useful to discriminate the different rock units and to measure the tectonic offset along the study fault segment. ASTER datasets were examined and processed using ENVI (version 5.3) and Arc GIS Desktop (version 10) software packages.

Gad and Kusky (2006) 7-3-1 in RGB band combination have been firstly applied. It is worth noting that other band combinations have been tested, but results from these other combinations did not offer many details for the different lithological units along the Erkenek Segment. Therefore, the authors explored some of the widely used band rationing techniques for lithological mapping because of their proven ability to enhance rock compositional differences (Mustard and Sunshine 1998).

The optimal bands for band ratio images have been selected according to; (1) Optimum Index Factor, OIF; that is a statistical approach for detecting the maximum ranking of combinations of three channels out of the spectral bands (Chavez et al. 1982) and (2) the spectral properties of the surface material of interest and its abundance in comparison with to other surface cover types (Sabine 1999; Gad and

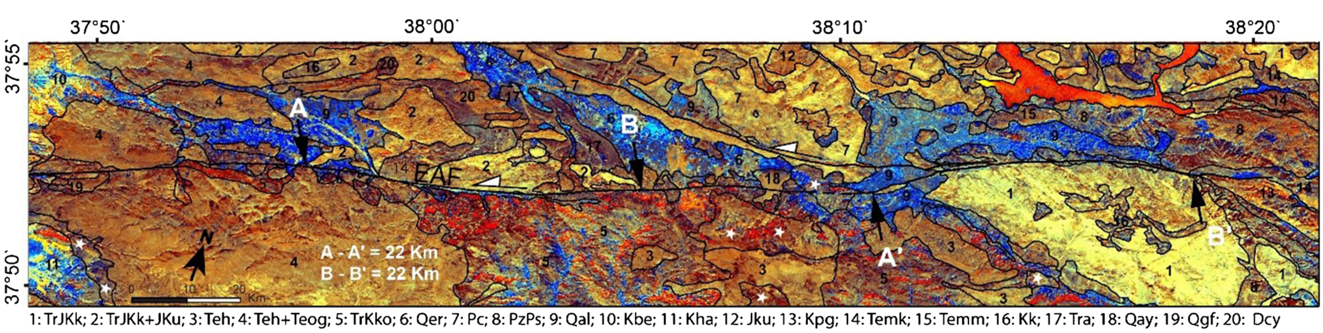

Fig. 5 ASTER band ratio image (1/3-1/9-3/9) in RGB. White stars indicate the landslide

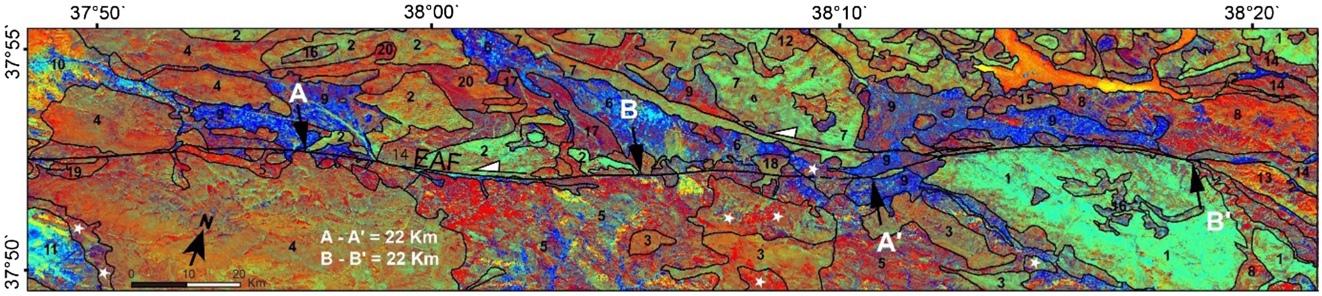

Fig. 6 ASTER band ratio image (7/3-1/7-3/5) in RGB

Kusky 2007), and also, depende on the selection of bands that carry the greatest variance with the least correlation (Jensen 1996; Gad and Kusky 2007).

Results and discussion

Results from Gad and Kusky (2006) bands 7-3-1 in RGB band combination displayed a clear distribution of some lithological units such as the Kayaköy Formation in northeastern part of the study area (Fig. 4). In southeastern part of the study region, the polygon coverage area of Hoya and Gaziantep formations is discriminated by this band combination as well (Fig. 4). Within this combination, the alluvial deposits are also well represented to occupy the most northern part of the study area (Fig. 4).

ASTER band ratio image 1/3-1/9-3/9 in RGB represents the highest optimum index factor (OIF) and indicative of spectral characters. Interpretation of this ASTER band ratio image clearly shows that this combination provides the best resolution in identification of different lithological units and their contacts when it is compared with the standard ASTER band combinations. It is worth noting that this is the first remote sensing study for the Erkenek Segment, which uses the ASTER images' band ratios 1/3-1/9-3/9 (Fig. 5), 7/3-1/7-3/5, and 9/5-5/3-3/1 (Figs. 6 and 7, respectively).

In this study, the main lithological units of the study area were successfully differentiated and identified as follows (Fig. 5): (1) the Kayaköy Formation (Fig. 5, polygon no. 1) that is located in the northeastern part of the study region and is represented with light yellow color; (2) the part made of both Kayaköy and Ula formations (Fig. 5, polygon no. 2) is accepted as a single unit, and this unit is well differentiated from the adjacent rocks in the northwestern parts with its yellow color; (3) Hoya Formation (Fig. 5, polygon no. 3) is characterized with its brown color to the south of the fault; (4) Hoya and Gaziantep formations (Fig. 5, polygon no. 4) together form the biggest unit of the study region, mostly distributed to its western parts, and are distinguished by reddish brown color; (5) Cherty limestone and basalts (Fig. 5, polygon no. 5) cover relatively a big area in the southern-central part of the fault segment and are well separated from the adjacent rocks with its yellowish red color; (6) conglomerate and sandstone (Fig. 5, polygon no. 6) is well represented and located as an elongated body with yellowish blue color in the northern-central part; (7) recrystallized limestone (Fig. 5, polygon no. 7) is discriminated by yellowish brown color and located in the middle northern part of the study area; (8) Pütürge metamorphics (Fig. 5, polygon no. 8) is distinguished with a dark blue color at both the eastern and western parts of the study area; (9) the alluvium (Fig. 5, polygon no. 9); and (10) Berit metaophiolite and Hatay ophiolite (Fig. 5, polygon nos. 10 and 11) occupy relatively small areas at the most northeastern and southeastern corners of the study area, respectively.

Results from the ASTER band ratio images clearly highlighted the geological offsets along the Erkenek Fault Segment at two points: (1) the one within the Kayaköy Formation in the southern part of the fault and (2) the one within the Kayaköy and Ula formations in the northern part. We measured a total of 22 km sinistral displacement between piercing points A-A′ and B-B′ at both of these localities (Fig. 8).

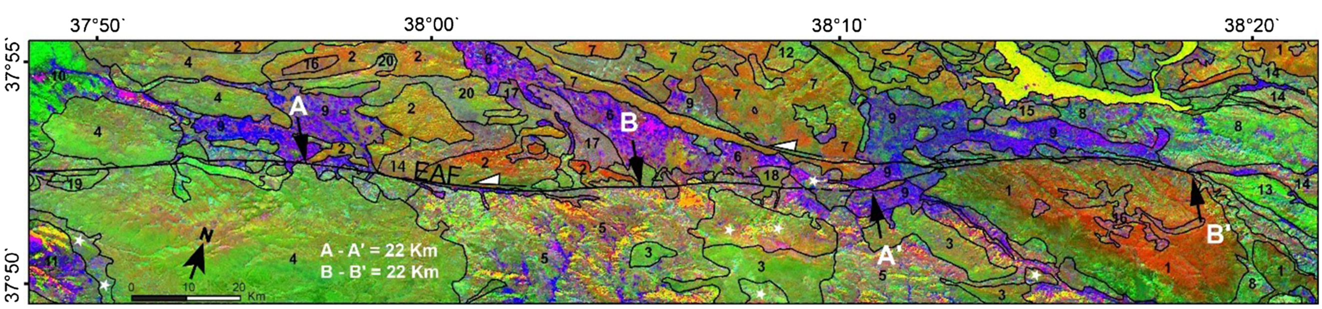

Fig. 7 ASTER band ratio image (9/5-5/3-3/1) in RGB

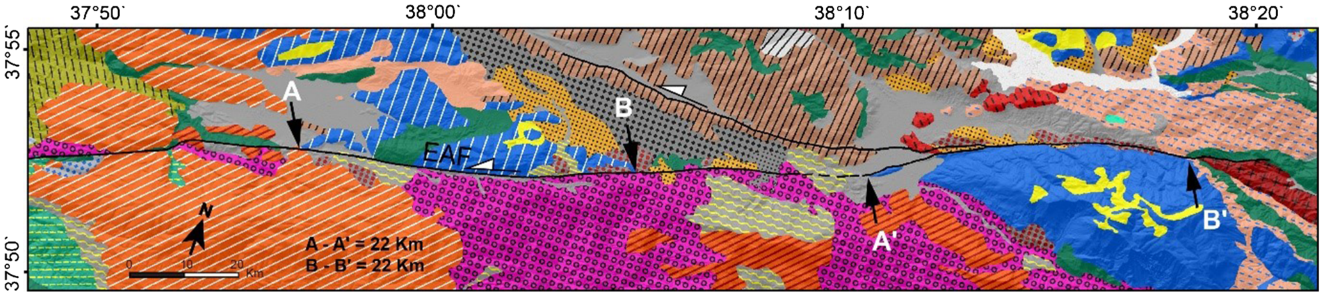

Fig. 8 Refined lithological map obtained in this study

Correlation between the previously published geological maps (e.g., Herece 2008) and our ASTER-based results supports the use of the newly adopted remote sensing technologies using ASTER images in accurate lithological mapping. Calc-schist, schist, and marble units are clearly discriminated from the surrounding rocks in our analysis (Fig. 8), whereas these lithological units are mapped as the conglomerate, sandstone, and mudstone units in the Herece's (2008) map (as Qer in Fig. 3). Also, the claystone with mudstone (Fig. 8) is neatly separated from the unit of Kayaköy and Ula formations (polygon no. 2) in the Herece's (2008) map. Geological offsets between A-A′ and B-B′ are found both to be 22 km, while they are suggested to be 22.5 km and 26 km, respectively, in Herece's (2008) geological map (Figs. 2 and 8), which indicate the consistency of the offset results using the advanced remote sensing techniques used in the lithological mapping of the study area.

Conclusion

The results obtained from ASTER image interpretations are consistent with the published Herece's (2008) geological map in a large scale. This indicates that combining a high-resolution ASTER data with other field information is positive and appropriate for detailed lithological mapping. The evaluation of the newly developed ASTER band ratio technique proved to be a strong tool for lithological mapping and in checking the recorded geological offsets along the Erkenek Segment of the EAF. It is clear that the ASTER band ratio images of bands 1/3-1/9-3/9, 7/3-1/7-3/5, and 9/5-5/3-3/1 in RGB are powerful in discriminating the subtle contacts between the different lithological units along the Erkenek Segment. The ASTER band ratio images also measure the geological offsets as 22 km at the examined locations along the Erkenek Segment. The new band ratio images are adjusted to discriminate between various rock units and formations of pre-Miocene age. Therefore, it is recommended for detailed lithological mapping and active fault offset measurements along other regions of the same criteria. We suggest ASTER image enhancement techniques as time- and cost-effective methods for detailed lithological mapping along active fault regions of similar conditions.

Acknowledgments The authors are very thankful to Cengiz Zabcı, Istanbul Technical University, for his suggestions and kind significant discussion to improve this work.

References

Abdeen MM, Allison TK, Abdelsalam MG, Stern RJ (2001) Application of ASTER band-ratio images for geological mapping in arid regions; the Neoproterozoic Allaqi Suture, Egypt. Annual meeting of Geological Society of America (Abstract), Boston, Massachusetts, November: 5–8, p. 289

Aktuğ B, Özener H, Dogru A, Sabuncu A, Turgut B, Halicioglu K, Yilmaz O, Havazli E (2016) Slip rates and seismic potential on the East Anatolian Fault system using an improved GPS velocity field. J Geodyn 94–95:1–12

Bacheri I, Hakdaoui M, Raji M, Teodoro AC, Benbouziane A (2019) Machine learning algorithms for automatic lithological mapping using remote sensing data: a case study from Souk Arbaa Sahel, Sisi Ifni inlier, Western Anti-Atlas, Morocco. ISPRS Int J Geo Inf 8(6):248

Bedell RL (2001) Geological mapping with ASTER satellite: new global satellite data that is a significant leap in remote sensing geologic and alteration mapping. Special Publications, Geological Society of Nevada 33:329–334

Chavez PS, Berlin GL, Sowers LB (1982) Statistical methods for selecting of Landsat MSS ratios. J Appl Photogr Eng 8:30–32

Dewey JF, Hempton MR, Kidd WSF, Saroglu F, Şengör AMC (1986) Shortening of continental lithosphere: the neotectonics of Eastern Anatolia–a young collision zone. In: Coward MP, Ries AC (eds) Collision Tectonics. Special Publications, Geological Society of London, vol 19, pp 3–36

Duman TY, Emre Ö (2013) The East Anatolian Fault: geometry segmentation and jog characteristics. In: Robertson AHF, Parlak O, Ünluüginç UC (eds) Special Publications, Geological Society of London, vol 372, pp 495–529

Farr TG, Rosen PA, Caro E et al (2007) The shuttle radar topography mission. Rev Geophys 45:1–33

Gabr SS, Hassan SM, Sadek MF (2015) Prospecting for new gold bearing alteration zones at El-Hoteib area. South Eastern Desert, Egypt, using remote sensing data analysis. Ore Geol Rev 71:1–13

Gad S, Kusky TM (2006) Lithological mapping in the Eastern Desert of Egypt, the Barramiya area, using Landsat thematic mapper (TM). J. Afr. Earth Sci. 44:196–202

Gad S, Kusky TM (2007) ASTER spectral ratioing for lithological mapping in the Arabian-Nubian shield, the Neoproterozoic Wadi Kid area, Sinai, Egypt. Gondwana Research 11:326–335

Gürsoy Ö, Kaya Ş, Çakır Z, Tatar O, Canbaz O (2017) Determining lateral offsets of rocks along the eastern part of the North Anatolian Fault Zone (Turkey) using spectral classification of satellite images and field measurements. Geomatics Nat Hazard Risk 8:13–25

Hempton MR (1985) Structure and deformation history of Bitlis suture near Lake Hazar, southeastern Turkey. Bull Geol Soc Am 96:233–243

Herece E (2008) Atlas of the East Anatolian Fault (1:500,000). General Directorate of Mineral Research and Exploration of Turkey (MTA), Ankara, Turkey. Special Publication Series 13:13,359

Hewson RD, Cudahy TJ, Huntington JF, (2001) Geologic and alteration mapping at Mt Fitton, South Australia, using ASTER satellite-borne data. International Geosciences and Remote Sensing Symposium (Conference Paper), February 2:724–726

Hubert-Ferrari A, King G, Vander Woerd J, Villa I, Altunel E, Armijo R (2009) Long-term evolution of the North Anatolian Fault: new constrains from its eastern termination. In: Van Hinsbergen, D. J. J., Edwards M. A. and Govers, R., (eds). Collision and collapse at the Africa-Arabia-Eurasia Subduction zone. Special Publications, Geological Society of London 311:133–154

Ibrahim WS, Watanabe K, Yonezu K (2016) Structural and litho-tectonic controls on Neoproterozoic base metal sulphide and gold mineralization in north Hamisana shear zone, south eastern desert, Egypt: the integrated field, structural, land sat7 ETM+ and ASTER data approach. Ore Geol Rev 79:62–77

Iwasaki A, Tonooka H (2005) Validation of a crosstalk correction algorithim for ASTER/SWIR. IEEE Trans Geosci Remote Sens 43(12):2747–2751

Jensen J (1996) Introductory digital image processing: a remote sensing prospective, 2nd edn. Prentice-Hall, Englewood Cliffs

Khalifa A (2014) Landsat ETM+ digital image processing techniques for lithological enhancement, along Qena – Safaga road, Eastern Desert, Egypt (extended abstract), 67th EAGE Conference & Exhibition 2014, Amsterdam, RAI, June 16–19

Khalifa A (2018) Morphotectonic analysis of the East Anatolian Fault (E. Turkey) using remote sensing techniques. Dissertation, Istanbul Technical University

Khalifa A, Çakir Z, Owen A, kaya Ş (2018) Morphotectonic analysis of the East Anatolian Fault, Turkey. Turk J Earth Sci 27:110–126

Khalifa A, Çakir Z, Owen A, Kaya Ş (2019) Evaluation of the relative tectonic activity of the Adıyaman fault within the Arabian-Anatolian plate boundary (eastern Turkey). Geologicaacta 17(6):1–17

Liu L, Zhou J, Han L, Xu X (2017) Mineral mapping and ore prospecting using Landsat TM and Hyperion data, Wushitala, Xinjiang, northwestern China. Ore Geol Rev 81:280–295

Mars JC, Rawan LC (2010) Spectral assessment of new ASTER SWIR surface reflectance data products for spectroscopic mapping of rocks and minerals. Remote Sens Environ 114:2011–2025

McKenzie DP (1970) Plate tectonics of the Mediterranean region. Nature 220:239–343

Meghraoui M, Bertrand S, Karabacak V, Ferry M, Çakir Z Altunel E (2006) Surface ruptures along the Maras segment of the East Anatolian Fault (SE Turkey) and kinematic modelling from Tectonic and GPS data. European Geosciences Union, General Assembly, (Abstract), Vienna, Austria, April 2–7; 8, 10006. 1607–7962/gra/EGU06-A-10006

Mustard JF, Sunshine MJ (1998) Spectral analysis for earth science: investigations using remote sensing data. In: Rencz AN (ed) Remote Sensing for the Earth Sciences: Manual for Remote Sensing, vol 3, pp 251–306

Nemmour-Zekiri D, Oulebsir F (2020) Application of remote sensing techniques in lithological mapping of Djanet region, eastern Hoggar Shield, Algeria. Arab J Geosci 13:632

Ninomiya Y, Fu B, Cudahy TJ (2005) Detecting lithology with advanced spaceborne thermal emission and reflection radiometer (ASTER) multispectral thermal infrared "radiance-at-sensor" data. Remote Sens Environ 99:127–139

Okada K, Ishii M (1993) Mineral and lithological mapping using thermal infrared remotely sensed data from ASTER simulator. International Geosciences and Remote Sensing Symposium "Better Understanding of Earth Environment", (Abstract), Tokyo, Japan, August 18–21, 93:126–128

Pour AB, Hashim M (2015) Geological structure mapping of the Bentong-Raub suture zone, peninsular Malaysia using palsar remote sensing data. Int Soc Photogramm Remote Sens 11-2(W2):89–92

Pour AB, Hashim M, Van Genderen J (2013) Detection of hydrothermal alteration zones in a tropical region using satellite remote sensing data: Bau gold field, Sarawak, Malaysia. Ore Geol Rev 54:181–196

Pour AB, Hashim M, Park Y, Hong JK (2018a) Mapping alteration mineral zones and lithological units in Antarctic regions using spectral bands of ASTER remote sensing data. Geocarto Int 32(12):1281–1306

Pour AB, Park Y, Park TS, Hong JK, Hashim M, Woo J, Ayoobi I (2018c) Regional geology mapping using satellite-based remote sensing approach in Northern Victoria Land, Antarctica. Polar Science 16:23–46

Pour AB, Park TS, Park Y, Hong JK, Zoheir B, Pardhan B, Ayoobi I, Hashim M (2018d) Application of multi-sensor satellite data for exploration of Zn-Pb sulphide mineralization in the Franklinian Basin, North Greenland. Remote Sens 10:1186

Pour AB, Hashim M, Hong JK, Park Y (2019) Lithological and alteration mineral mapping in poorly exposed lithologies using landsat-8 and ASTER satellite data: north-eastern Graham Land, Antractic Peninsula. Ore Geol Rev 108:112–133

Rajendran S, Nasir S, Kusky TM, Ghulam A, Gabr S, El-Ghali MA (2013) Detection of hydrothermal mineralized zones associated with listwaenites in Central Oman using ASTER data. Ore Geol Rev 53:470–488

Reilinger R, McClusky S, Vernant P, Lawrence S, Ergintav S, Cakmak R, Ozener H, Kadirov F, Guliev I, Stepanyan R, et al (2006) GPS constraints on continental deformation in the Africa-Arabia-Eurasia continental collision zone and implications for the dynamics of plate interactions. J Geophys Res Solid Earth 111:1–26

Rowan LC, Mars JC (2003) Lithologic mapping in the mountain pass, California area using advanced spaceborne thermal emission and reflection radiometer (ASTER) data. Remote Sens Environ 84:350–366

Rowan L, Hook SJ, Abrams MJ, Mars JC (2003) Mapping hydrothermally altered rocks at cuprite, Nevada, using the advanced spaceborne thermal emission and reflection radiometer (ASTER), a new satellite-imaging system. Econ Geol 98(5):1019–1027

Sabine C (1999) Remote sensing strategies for mineral exploration. In: Rencz AN (ed) Remote Sensing for the Earth Sciences, Manual of Remote Sensing, vol 3, pp 375–447

Safari M, Maghsodi A, Pour AB (2017) Application of Landsat 8 and ASTER satellite remote sensing data for porphyry copper exploration: a case study from shear-e-Babak, Kerman, south of Iran. Geocarto Int 33(11):1186–1201. https://doi.org/10.1080/10106049.2017.1334834

Şengör AMC, Görür N, Şaroğlu F (1985) Strike slip faulting and related basin formation in zones of tectonic escape: Turkey as a case study. In: Biddle KT, Christie-Blick N (eds) Strike-slip deformation, basin formation and sedimentation, Society of Economic Paleontologists and Mineralogists, vol 37, pp 227–264

Sheikhrahimi A, Pour AB, Pardhan B, Zoheir B (2019) Mapping hydrothermal alteration zones and lineaments associated with orogenic gold mineralization using ASTER data: a case study from the Sanandaj-Sirian zone, Iran. Adv Space Res 63:3315–3332

Velosky JC, Stern RJ, Johnson PR (2003) Geological control of massive sulfide mineralization in the Neoproterozoic Wadi Bidah shear zone, southwestern Saudi Arabia, inferences from orbital remote sensing and field studies. Precambrian Res 123(2–4):235–247

Yamaguchi Y, Naito C (2003) Spectral indices for lithologic discrimination and mapping by using the ASTER SWIR bands. Int J Remote Sens 24(22):4311–4323

Yamaguchi Y, Kahle AB, Kawakami T, Paniel M (1998) Overview of the advanced spaceborne thermal emission and reflection radiometer (ASTER). IEEE Trans Geosci Remote Sens 36(4):1062–1071